

www.acsanm.org Article

Characterizing Bismuth Doping of Colloidal Germanium Quantum Dots for Energy Conversion Applications

Heather Renee Sully, Katayoon Tabatabaei, Kaitlin Hellier, Kathryn A. Newton, Zheng Ju, Logan Knudson, Shayan Zargar, Minyuan Wang, Susan M. Kauzlarich, Frank Bridges, and Sue A. Carter*



Cite This: https://dx.doi.org/10.1021/acsanm.0c00709



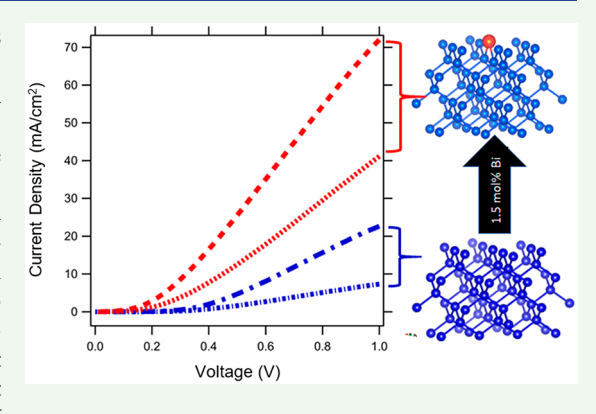
ACCESS

Metrics & More

Article Recommendations

Supporting Information

ABSTRACT: The numerous electronic and optoelectronic applications that rely on semiconductors require tuning their properties through doping. Germanium quantum dots (Ge QDs) were successfully doped with bismuth up to 1.5 mol %, which is not achievable in the bulk Ge system. The structures of oleylamine- and dodecanethiol-capped Ge QDs were probed with EXAFS, and the results are consistent with Bi dopants occupying surface lattice sites. Increasing the amount of Bi dopant from 0.50 to 1.5 mol % results in increasing disorder. In particular, the nearestneighbor Bi—Ge bond length is much longer than the Ge—Ge bond length in Ge QDs. Oleylamine to dodecanethiol ligand exchange was shown to partially restore order in doped QDs. Transport measurements of the Bidoped Ge QD thin films revealed that Bi doping leads to a significant increase in dark current and photocurrent. These results indicate that doping can provide a pathway for improving the performance of group IV



quantum dots for energy conversion applications including photodiodes and photovoltaic cells.

KEYWORDS: germanium, quantum dots, bismuth, doping, EXAFS

■ INTRODUCTION

Colloidal semiconductor quantum dots (QDs) have the potential to replace their bulk counterparts by eliminating high-temperature, high-energy processes to produce large-area, flexible, and solution-processed thin film arrays. ¹⁻³ Bulk germanium (Ge) has a high carrier mobility, important for transport, and a high absorption coefficient. ⁴⁻⁷ The narrow and desirable bandgap (0.67 eV at 300 K) makes Ge nanomaterials a candidate for IR detectors and as a tandem material for photovoltaics. Ge QDs offer a low-toxicity alternative to heavy-metal-containing QDs such as CdTe and PbS, and the large Bohr excitation radius of ~24 nm results in a wide range of bandgap tunability.

Electronics and optoelectronics, such as diodes, solar cells, and transistors, depend on tuning the properties of bulk semiconductors by doping with heterovalent atoms. To realize the potential for QDs as the active layer in electronic devices such as photodetectors, LEDs, solar cells, and memory, increasing charge carrier density is critical as charge transport in pure QDs is inherently limited. As with bulk semiconductors, doping is the primary way to tune electronic or optical properties and increase the concentration of charge carriers. Anny compound semiconductors QDs have been the focus of these efforts such as CdSe, InAs, and PbS. 10,11,16

Several synthetic methods have been used to fabricate QDs, including chemical vapor deposition (CVD), molecular beam

epitaxy (MBE), and gas phase synthesis.7,17-20 Solution synthesis has several advantages: the use of common reagents, scalability, and production of suspended colloids which can be transferred into various solvents. Kinetically controlled crystal growth and altered chemistry due to the high surface to volume ratios are known to make the synthetic chemistry of doping QDs different from that of the bulk counterparts. 11,21,22 A fundamental understanding of crystallization of elemental QDs with doping is still in development, as many elemental systems have unique synthesis characteristics. Halide precursors can be reduced in the presence of a capping agent, ^{23–25} and the mixed valence reduction method has been used to produce both Si and Ge QDs. 25-27 Doping is accomplished during synthesis by employing an additional halide precursor that contains the desired doping element and can be co-reduced and incorporated into the lattice. For example, PCl₃ and SiCl₄ co-reduced with Mg in 1,2-dimethoxyethane produce P-doped Si nanocrystals. 18,28 Ruddy et al. synthesized Ge QDs with group III, IV, and V dopants to increase n- and p-type character. Although elemental

Received: March 20, 2020 Accepted: May 1, 2020 Published: May 1, 2020



analysis showed compositions ranging from 0.91 to 1.4 mol % dopant, the QDs lacked free charge carriers and had a negligible increase in conductivity. Other groups were able to detect changes in the conductivity of Ge QDs doped with transition metals and main-group elements. 19,29,30

In this work, we investigate the structure and electronic enhancement of Bi n-type doping into Ge QDs synthesized using a low-temperature microwave-assisted solution route as reported in previous work by Tabatabaei et al. Bi is a large atom with no solubility in bulk Ge, yet it is detected in Ge QD samples even after ligand exchange. This is similar to Ge—Sn alloy nanomaterials. Like Bi, Sn is a large atom with no solubility in Ge. Ge—Sn thin films have been investigated for strain-induced transition of Ge from an indirect to direct band transition. By the same mechanism, a strain-induced direct band transition has been theorized for Ge—Bi. To achieve this, Bi must be incorporated into the host material and not physisorbed on the surface or clustered, making dopant location of great importance.

The high surface area of nanomaterials distinguishes them from bulk counterparts, which is an important consideration when characterizing dopant location. Oliva-Chatelain et al. categorized dopants as c-type when the dopant is inside the crystal, s-type when the dopant is on the surface, and m-type when the dopant is in the matrix, which applies to QDs in a solid matrix such as SiO₂ or when capping ligands contain the doping atom. The authors point out that these dopant types can coexist and that they may act in different ways. The s-type doping may be substitutional or weakly bound to the surface. 18 Although they have a small atomic radius compared to Ge, phosphorus (P) and boron (B) dopants in Ge nanocrystals were found to occupy the surface of QDs synthesized via a nonthermal plasma. ^{7,19} In any of these locations, dopants may be present but not electronically active in the intended way of contributing charge carriers to current in the material. First, to contribute to charge carriers, the doping atoms must also be shallow dopants that ionize easily. ^{1,21,34,35} Second, dopants may phase segregate, bonding to other dopant atoms instead of host atoms, or act as recombination centers if there is high disorder around dopant atoms. 15 Previous work on microwave-assisted synthesis Bidoped Ge QDs demonstrated that Bi is present in the QD samples.⁵ Because the nature of dopant incorporation into the structure is important for understanding the transport and optoelectronic properties, this work further investigates the structure effects of Bi inclusion into Ge QDs.

Dopant concentration must be kept low to prevent transition from the semiconductor to the semimetal. 18 The samples reported in this work have Bi dopant concentrations between 0.5 and 1.5 mol %, corresponding to $10^{20}-10^{21}$ Bi atoms per cm³. Characterizing low percentage dopants in colloidal QDs is challenging, especially for nonfluorescing elements such as Ge. The dopant signal is often undetectable and limited to elemental analysis. 8,21,29,35 Some groups have determined the location of dopants in Ge QDs by oxidizing and etching their material. However, this does not give information about how dopants are incorporated into the host crystal. 7,19 Extended X-ray absorption fine structure (EXAFS) provides element specific local structure information including the number of nearest neighbors, bond length, and disorder. Besides distinguishing amorphous versus crystalline character of nanoparticles, 36 EXAFS can distinguish dopant clustering from lattice incorporation by differentiating between the species of the nearest neighbor atoms.³⁷ With EXAFS and reverse Monte Carlo simulations, Winterer et al.

found Ag to occupy distorted interstitial sites in CdSe nanocrystals. ²¹ In Gul et al., ZnSe nanocrystals were doped with Cu which resided on the host lattice near the particle surfaces revealed by EXAFS analysis. ³⁸ In contrast, Sb and In were found to be substitutional in PbS nanocrystals studied by Konstantatos et al. ¹⁵

Although, the majority of our focus was on dopants, we also considered the effect of ligand molecules on disorder. The high surface area of QDs requires surface functionalization with ligand molecules in order for colloidal QDs to be soluble. In addition, the type of ligand is important for functionalization as it affects the chemical, electrical, and optical behavior. 41 The effect of ligand-induced surface dipoles on energy levels of PbS and CdSe QDs has been studied and presents an understanding based on electrostatic considerations. 42-45 Less explored is the relationship between structural disorder and ligands or ligand exchange due to the limited techniques for determining the atomic arrangement of nanomaterials. Surface atoms are susceptible to disorder-induced trap states and deviation from expected crystal bond lengths. Various ligand molecules will induce different electron sharing based on their molecular properties which can reorder the surface structure of QDs through bond length modification. Alternatively, the process of ligand exchange puts QD surface atoms in a state of undercoordination and then restored coordination with heat treatment. Ligand exchange for ZrO2 nanocrystals was found to induce strain rearrangement which decreased structural disorder. 46 Ligand exchange processing as a pathway to reduce QD disorder presents an opportunity to further the development of functional nanomaterials.

In this work, EXAFS was used to investigate dopant incorporation into the Ge crystal lattice and lattice disorder around Bi atoms in Ge QDs before and after ligand exchange. Photothermal deflection spectroscopy (PDS) measured disorder, and conductivity measurements provided further insight into dopant and ligand effects. Lastly, photodiode devices were fabricated, and current density—voltage measurements were taken under a calibrated 1-sun solar simulation.

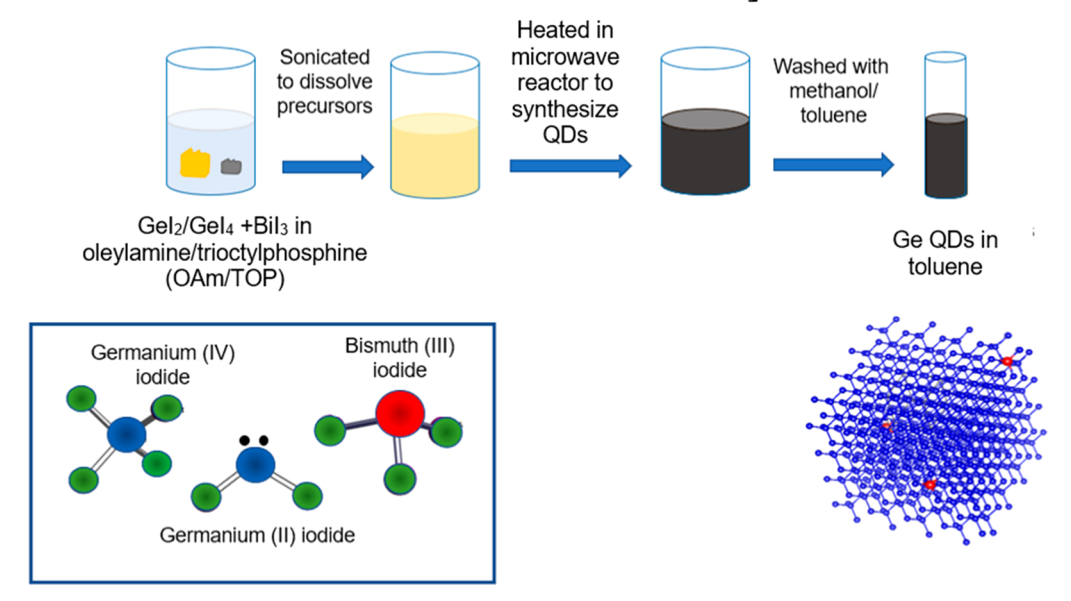
EXPERIMENTAL METHODS

QD Synthesis and Ligand Exchange. Pure and doped Ge QD were prepared according to a previously published method. Siriefly, 0.40 mmol of GeI_2 or $\mathrm{GeI}_2/\mathrm{GeI}_4$ with the total Ge content held at 0.40 mmol and BiI_3 (0.5–1.5 mol %) were dissolved in either 8 mL of oleylamine (OAm) or a mixture of 7 mL of OAm and 1 mL of trioctylphosphine (TOP) and heated in a CEM Discover microwave reactor to 250 °C for an hour. The resulting particles, which are passivated with OAm or OAm/TOP, were precipitated with toluene as a nonpolar solvent and methanol as a polar nonsolvent and suspended in toluene. Large, pure QDs were prepared by using 0.1 mmol of GeI_4 and 4 mL of OAm in a 35 mL microwave tube. The solution was heated at 250 °C for an hour and 45 min, cooled to room temperature, and then heated at 260 °C for 15 min.

Ligand exchange was performed by first removing surface ligands by adding 5 mL of 5 M hydrazine solution in acetonitrile to the QD toluene solution. The mixture was stirred at room temperature for an hour before being precipitated with toluene and methanol. We applied several washing and centrifugation (8500 rpm) cycles using toluene, hexane, acetonitrile, and methanol to ensure complete removal of OAm. The QDs were then added to 10 mL of dodecanethiol (DDT) and heated for 60 min at 150 °C in a CEM Discover microwave. The DDT-capped QDs were isolated and washed with toluene and methanol and redispersed in toluene. To prepare sulfide-capped Ge QDs, 5 mL of 80 mM sodium sulfide solution in formamide was added to a 5 mL toluene dispersion of QDs, and the mixture was stirred at

Scheme 1. The Microwave-Assisted QD Synthesis (Steps, Precursors, and Product) Used to Fabricate the Samples Studied

Microwave-Assisted QD Synthesis



room temperature overnight. The phase transfer of QDs from the dark brown top toluene layer to the colorless formamide bottom layer qualitatively indicated a successful ligand exchange. The QDs were separated by discarding the colorless toluene layer, followed by washing the formamide layer multiple times with acetonitrile and hexane and centrifuging at 8500 rpm for 20 min. The QD precipitate was suspended in formamide for further use. Successful ligand exchange was confirmed by FTIR analysis, shown in the Supporting Information (Figure S1).

Materials Characterization. Transmission Electron Microscopy. Samples for both high-resolution transmission electron microscopy (TEM) and scanning transmission electron microscopy (STEM) were prepared by drop-casting dilute toluene dispersions of Ge QDs onto lacey carbon supported by a 400 mesh copper grid (Ted Pella). The grids were dried overnight at room temperature and then overnight at 80 °C in an oven to minimize carbon contamination during electron beam irradiation. QDs were imaged at 200 keV in STEM/TEM mode with an aberration-corrected JEOL JEM-2100F/Cs equipped with Gatan annular dark field (ADF) and bright field detectors. To determine the average particle size and respective standard deviation, 200–250 individual NCs were measured from different regions of each sample. Particle sizes were determined by using the ImageJ software package.

X-ray Absorption Spectroscopy. QD's were deposited onto a filter paper $(3 \times 12 \text{ mm}^2)$ such that the step height at the Ge K edge was roughly 0.5 and were sealed with a thin layer of Scotch Magic tape. EXAFS data were collected at the Stanford Synchrotron Radiation Lightsource (SSRL) on beamline 4-1 for bulk Ge powder, pure Ge QD, and Bi-doped Ge QD samples, in fluorescence mode at the Bi L₂ edge (the Bi L₃ fluorescence overlaps the stronger Ge K_{β} and cannot be used) and in transmission mode at the Ge K edge.

Spectra were collected at a temperature below 10 K in an Oxford helium cryostat by using a 220 monochromator; at the Bi L_2 edge a vertical slit size of 0.3 mm provided an energy resolution of 4.0 eV. The Bi L_2 edge is at 15711 eV, and the monochromator was detuned to 70% at 15900 eV. For Ge, the edge is at 11100 eV, and the monochromator was detuned at 11300 eV; with a vertical slit size of 0.4 mm, the energy resolution was 1.9 eV.

EXAFS oscillations were extracted from the absorption data and transformed by using the RSXAP package, 47 which includes pre- and post-edge background subtraction, step height normalization, and removal of glitches in the Bi $\rm L_2$ edge fluorescence. The Bi $\rm L_2$ edge was used because the intense Ge $\rm K_{\beta}$ fluorescence overlaps the Bi $\rm L_3$

fluorescence. The spectra were then transformed into k-space (see Experimental Methods and Figure S2) and fast Fourier transformed into real space. In r-space, the fast oscillating function is the real part R of the FFT and provides a measure of the phase, while the envelope functions are $\pm \sqrt{R^2 + I^2}$, with I being the imaginary part of the FFT. An FT window of 4–10.5 Å $^{-1}$ and 3.5–15 Å $^{-1}$, Gaussian rounded by 0.2 Å $^{-1}$, were used for the Bi and Ge edge respectively. The fit range was 1.9–4.5 Å for both edges.

Fits of the data were performed in r-space to a sum of theoretical functions calculated by using the code FEFF7. For the Bi edge, our model initially substituted a Bi atom on an undistorted Ge lattice site. Large bond length expansions were allowed to account for the larger covalent radius of Bi relative to Ge. In general, the amplitude is given by NS_0^2 , where N is the number of neighbors and S_0^2 is an amplitude reduction factor. Using bulk Ge, we determined that S_0^2 is very close to 1.0 for Ge data; S_0^2 was also set to 1 for the Bi data. The amplitude is also correlated to the width of the pair distribution function, σ , and that leads to absolute uncertainties on the order of 10-20% for N and σ^2 . Fits included the first three Ge neighbors about Bi. In some cases, extra structure occurs near the first peak, and additional Bi—Bi or Bi—O peaks were included; see the Supporting Information for further details.

Photothermal Deflection Spectroscopy (PDS). Samples were prepared in a nitrogen glovebox by drop-casting solutions of colloidal QDs onto glass slides. Samples were then immersed in Fluorinert FC-72 (perfluorohexane) inside a glass cuvette for data collection.

Light from a tungsten halogen arc lamp was used to pump the sample. The light was chopped at 5 Hz and scanned from 450 to 2100 nm by using a Princeton Instruments Acton monochromator. The light was focused on the sample using tabletop optics and with a full width half-maximum of 15 nm. A JDSU helium—neon 633 nm laser was aligned parallel to the surface of the sample and used as a probe beam. As the modulated pump beam excited the sample, heat from nonradiative relaxation caused the probe beam to be deflected. The deflection was registered with a Thorlabs PDP90 position-sensitive detector. Lock-in amplifiers allow for high-sensitivity absorption measurements. The absorbance is given by the expression $\alpha = -\frac{1}{d} \ln(1 - \frac{V_{\rm sig}}{V_{\rm ref}} C_{\rm norm})$, where d is the sample thickness, $V_{\rm sig}$ is the signal amplitude, $V_{\rm ref}$ is the signal from the reference detector, and $C_{\rm norm}$ is the

Conductive Atomic Force Microscopy (C-AFM). Topography and current images were obtained with a Bruker Dimension Icon system in

normalization constant.

tapping mode. A Bruker DDESP-V2 antimony-doped silicon cantilever tip was used. The cantilever was made with reflective aluminum backside, and the conductive diamond front side was used and had a spring constant of 80 N/m. QD films were fabricated by spin-casting toluene dispersions on ITO-coated glass substrates, and silver paste was used to make contact. Current measurements were taken under 100 mV in ambient conditions in tapping mode to prevent QD displacement on the substrate by the AFM tip. Gwyddion⁴⁹ software was used for processing and image formatting.

Device Fabrication. Glass substrates patterned with ITO electrodes were spin-cast with ${\rm TiO_2}$ sol—gel and ${\rm TiO_2}$ nanoparticles to act as a charge separating layer and to prevent electrical shorts. ${\rm TiO_2}$ sol—gel was prepared by the standard procedure described previously. ODs capped with S²— were drop-cast onto these devices in a nitrogen glovebox and heated on a hot plate at 300 °C to evaporate the formamide solvent and form thin films. Silver films with a thickness of 90 nm were thermally evaporated under vacuum and served as the top electrode. Current density—voltage (J-V) curves were performed in a nitrogen-filled glovebox. Measurements were taken in the dark and under illumination calibrated to AM1.5G.

■ RESULTS AND DISCUSSION

QD Synthesis. The synthesis procedure is illustrated in Scheme 1 showing precursors, steps and a conceptualization of the product.

X-ray Absorption Fine Structure (EXAFS). The *r*-space data and fits are shown in Figure 1 for 0.50, 1.0, and 1.5 mol % Bi-

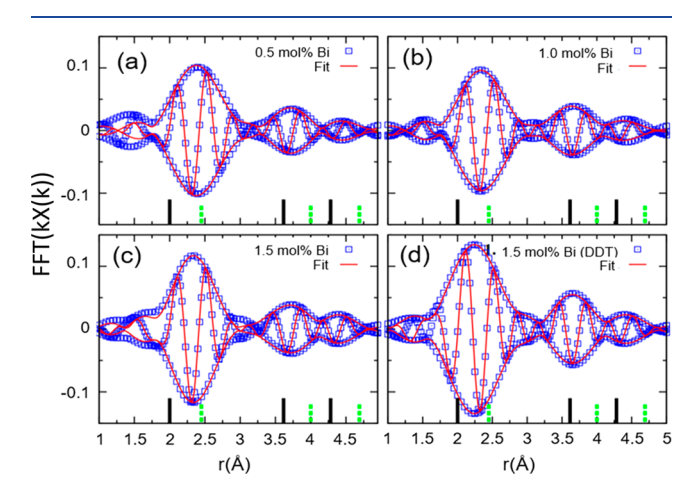


Figure 1. EXAFS data in *r*-space (points) and fits (red line) for (a) 0.50, (b) 1.0, and (c) 1.5 mol % Bi-doped Ge QDs; (d) 1.5 mol % Bi Ge QD sample at the Bi L_2 edge, recapped with DDT. In *r*-space data, the fast oscillating function is the real part R of the FFT and provides a measure of the phase, while the envelope function is $\pm \sqrt{R^2 + I^2}$, with I being the imaginary part of FFT. Green (dashed) lines indicate the calculated distances from diffraction of first, second, and third neighbors in bulk Ge. The black lines indicate the expected peak locations for these neighbors on an EXAFS spectrum for an undistorted lattice.

doped, oleylamine—trioctylphosphine (OAm/TOP)-capped QDs. The presence of second- and third-neighbor peaks indicates that Bi atoms have first, second, and third nearest neighbors and are part of an ordered structure.

Calculated distances for the Ge lattice were obtained from a crystallographic information file from the American Mineralogist Crystal Structure Database. ⁵¹ Fits of the data were performed in *r*-space to a sum of theoretical standards ⁵² for the first three Bi—Ge pairs and, for some samples, a small Bi—Bi or Bi—O peak (see Figure S3 for details).

Green (dashed) lines in Figure 1a—d mark the calculated distances of the neighboring atoms on the undistorted Ge diamond structure, while the black (solid) lines correspond to the shifted position of the EXAFS peaks for such a Ge lattice. The well-known shifts of the peaks on an EXAFS plot are due to phase changes that the photoelectron undergoes when it is ejected from the excited atom and when it backscatters from neighboring atoms. The shift of the observed peak positions relative to the black lines indicates how much the pair distance differs from the ideal Ge structure.

Table 1 reports the peak shifts and positions from these fits. Note the shift decreases with increasing pair distance between the dopant and second and third neighbor. The first peak in *r*-space for the three doped samples has a very large *r*-shift of 0.28 to 0.29 Å. Bi has a larger covalent radius than Ge by 0.28 Å, which matches well with the observed *r*-shift for the first neighbor peak. The decreasing *r*-shift distortion for the second and third peaks shows that the distortion induced by the large Bi atoms relaxes as distance to the Ge neighbors increases. This fits the model that the Bi atoms sit on a Ge lattice site, likely at the surface since larger distortions are possible there.

A small amount of Bi—Bi bonding was found only in the 0.50 mol % sample. The shape of the first peak is slightly different, particularly around 2.7 Å. A small Bi—Bi peak greatly improved the fit and yields the same bond length for the nearest-neighbor Bi—Ge pair as for the other samples. Figure S3a shows an overlay of the 0.50 and 1.0 mol % data. The 0.50 mol % sample has a peak that is shifted to higher *r*-values and reflects a change in shape. Figure S3b shows calculated paths for Bi—Bi and Bi—Ge in black (dashed) and in blue (dot-dashed), respectively, overlaid on the 0.50 mol % sample fit. Note that when a Bi—Bi peak is included, the position of the first Bi—Ge peak agrees well with the other samples. The small peak for the Bi—Bi path shifts the first peak to slightly higher *r*-values; constructive and destructive interference between peaks for Bi—Bi and Bi—Ge can enhance (at 2.5 Å) or suppress (at 3.3 Å) the amplitude.

Amplitude values measured for the Bi L2 edge of the QD samples are shown in Table 1. Fit constraints included setting the second and third number of neighbors equal to replicate bulk structure. Amplitude values for the different doping concentrations are slightly different. However, because of the correlation between the amplitude and σ , the width of the pair distribution function, we cannot distinguish changes in amplitude values that are less than 0.5 neighbors. The amplitude values are significantly lower than that of bulk Ge, listed in row 1 of Table 1. Two major factors contribute to this: first, surface effects and, second, disorder associated with dopant atoms. Surface atoms have roughly half the number of neighbors as atoms on the interior. Atoms very close to the surface, one atomic level deep, have four first neighbors but only six second neighbors. In bulk materials the signal contributed from surface atoms are insignificant compared to that from interior atoms. Because of the large surface-to-volume ratio in nanocrystals, the effect of surface atoms becomes substantial, and the average number of neighbors decreases even for pure QDs. Because of the large size of the Bi atom, and the lack of Bi substitution in bulk Ge, Bi can only bond to the QDs at the surfaces or interfaces. Incorporation of a fraction of the Bi in an amorphouslike phase would give a small, broadened contribution to the first peak and essentially no contributions to further neighbor peaks; this would lead to a reduced amplitude of all peaks.

For Bi atoms on the surface, the number of first neighbors should be 2 or 3 depending on which plane of atoms the Bi is

Table 1. Fitting Results for Bi Dopant Atoms from the Fits to the Bi L₂ Edge for Bi-Doped Ge QDs^a

	path					
sample	parameter	Bi-O (Bi ₂ O ₃)	Bi-Bi (metal)	Bi-Ge	Bi-Ge	Bi-Ge
bulk	amp	6	3	4	12	12
	R (Å)	2.392	3.007	2.450	4.008	4.691
0.50 mol %	amp		2.0	1.7	2.1	2.1
	σ^2		0.009	0.0040	0.0030	0.013
	R (Å)		3.17	2.74	4.10	4.10
	shift (Å)		0.16	0.29	0.09	0.03
1.0 mol %	amp			1.7	1.7	1.7
	σ^2			0.0040	0.0040	0.0080
	R (Å)			2.74	4.10	4.73
	shift (Å)			0.29	0.09	0.04
1.5 mol %	amp			2.4	2.1	2.1
	σ^2			0.0050	0.0040	0.0070
	R (Å)	2.35		2.73	4.10	4.75
	shift (Å)			0.28	0.09	0.06
1.5 mol % (DDT)	amp	1.3		3.0	4.1	4.1
	σ^2	0.002		0.0040	0.0040	0.0080
	R (Å)			2.73	4.08	4.70
	shift (Å)	-0.04		0.28	0.07	0.03

[&]quot;Amplitude (number of neighbors) and the Debye–Waller factor (σ^2 , units Å²) for three Bi–Ge paths and Bi–O and Bi–Bi metal where applicable. Fit amplitudes for the second and third peak were set equal, the third peak has a larger value for σ^2 . Pair distances (Bi–Ge, Bi–O, or Bi–Bi) and r-shift parameters, in Å for the first, second, and third neighbors are included.

attached to. The lower number of neighbors for x = 0.5 and 1.0 mol % could arise if a small fraction of Bi atoms are weakly chemisorbed at the QD surface in an amorphous-like phase, possibly within the OAm/TOP ligands which were part of the synthesis. This effect would cause a decrease in the average number of neighbors for Bi atoms. To probe this, the surface ligands were removed with hydrazine and followed by recapping with DDT ligands. The spectrum for the 1.5 mol % Bi recapped with DDT is shown in Figure 1d, and the amplitude values are reported in Table 1. Note the larger amplitude for all peaks and particularly the second peak at 3.7 Å compared to Figure 1a-c. The amplitudes in Table 1 for the 1.5% samples (with and without DDT capping) are consistent with all the Bi being incorporated into the QDs surface; the reduced amplitudes for the 0.5 and 1.0% samples indicate a smaller fraction of Bi in the QDs, roughly 70%.

Fits indicate that after ligand exchange Bi dopants remain incorporated into the Ge lattice, and pair distances match previous samples. The best fit included a small amount of Bi oxide. Oxygen likely bonds to Bi atoms as the fourth neighbor. Despite the presence of Bi—O, the coordination on the peaks for DDT-capped sample is higher than that of the initial OAm/TOP-capped samples as reported in Table 1. The results are a better match to the simulated amplitudes of Bi atoms on the surface of Ge, and it is likely that all the Bi is incorporated into the surface for this sample. This result is consistent with a fraction of Bi being in a disordered state outside of the Ge host lattice for the OAm/TOP-capped samples.

Two models can account for the results for the DDT-capped sample. If the ligand exchange process removed loosely attached Bi atoms bonded to one or two Ge atoms, then the coordination of the first and second nearest neighbors would increase following ligand exchange. Alternatively, the ligand exchange process could cause rearrangement of the Bi atoms, increasing their coordination. In either scenario, ligand exchange increases the local order around the Bi atoms.

The Ge K-edge EXAFS data and fits for pure and doped QDs are shown in Figure 2. Table 2 shows Ge amplitudes and QD crystallite sizes as calculated by Scherrer analysis of XRD patterns (shown in Figure S6).

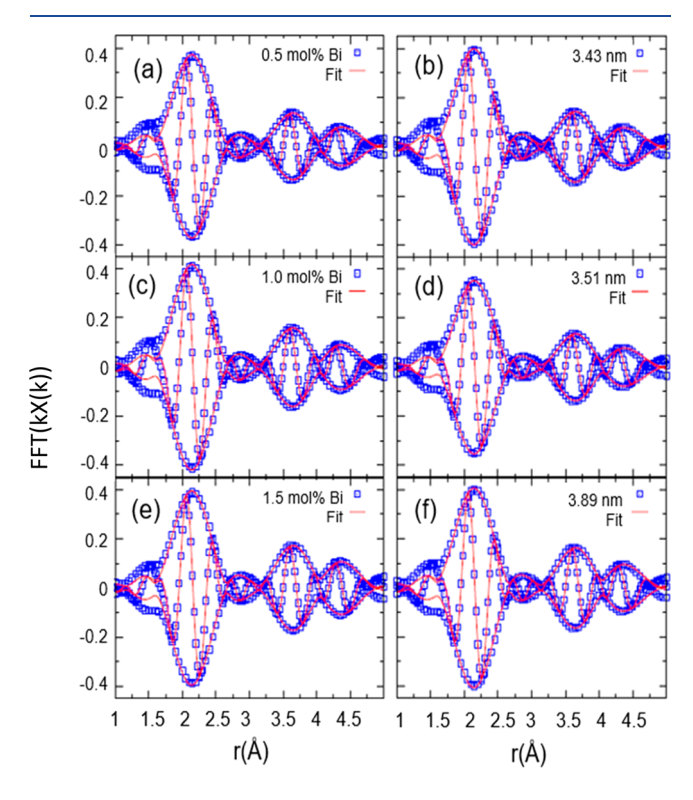


Figure 2. EXAFS data in *r*-space (points) and fits (red line) to the Ge K edge for the doped and pure QD samples. The FT range was 3.5-11.5 Å⁻¹, and the fit range was 1.9-4.6 Å. Doped sample spectra are shown in (a), (c), and (e), and pure sample spectra are shown in (b), (d), and (f). The crystallite size increases with doping and is reported in Table 2.

Table 2. Number of Neighbors around Ge from Fits to the Ge K Edge for Bulk Ge and OAm/TOP-Capped Pure and Doped QDs (Italic Values)

QD samples by size ^a (nm)	doping (mol % Bi)	Ge-Ge	Ge-Ge
bulk		4	12
3.43	0	3.0	6.5
3.51	0	3.3	6.8
3.89	0	3.4	7.2
9.7	0	3.6	8.4
3.5	0.5	3.2	6.9
5.0	1.0	3.5	8.2
8.6	1.5	3.4	8.8

^aCrystallite size as calculated from XRD patterns.

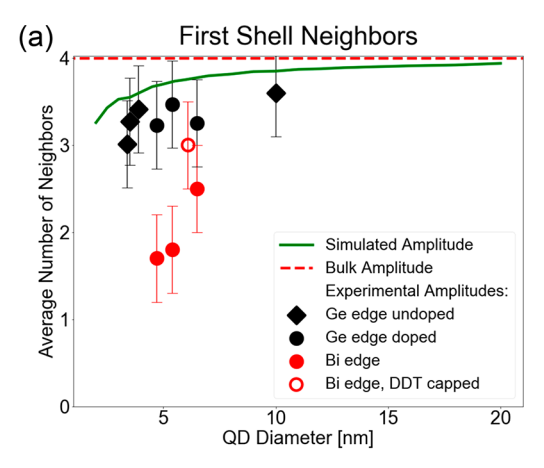
The fits show expanded Ge–Ge distances compared to the bulk reference, but the effects are small. The first-neighbor bond is expanded by roughly 0.007–0.009 Å, while the second-neighbor distance is expanded by 0.01–0.016 Å. Fits for the bulk sample have amplitudes close to 4 and 12 for the first and second neighbors, respectively (i.e., $S_0^2 \sim 1$), matching the expected values for the diamond cubic lattice. These results give us confidence in the fits presented here.

To understand whether the decrease in the Ge amplitude with decreasing crystallite size is purely a surface effect, the number of first and second nearest neighbors was simulated for QDs with diameters of 2–20 nm, as shown in Figure 3. Amplitudes from fits of the Ge edge of pure (black diamonds) and doped (black circles) are overlaid. Ge-edge experimental results follow the calculated trend and are within one standard deviation of the calculated values for the first shell. There may be an amorphous fraction in the samples; the relatively large amplitude observed for the first peak suggests that the maximum amorphous contribution is <20%.

Figure 4 shows representative high-resolution transmission electron microscopy (HRTEM) images of doped QDs, revealing faceted termination planes and grain boundaries. The equilibrium shape of inorganic nanocrystals contains facets as there is a minimization of exposed surface area. Both undoped and doped samples are found to be polycrystalline. The presence of grain boundaries necessitates the distinction between particle size and crystallite size for synthesized QDs. A particle may include multiple grains, while a crystallite is defined by a continuous grain orientation. The distinction is relevant because it is the size of the continuous grain, bordered by a grain boundary, which defines surface related disorder as quantified in EXAFS measurements. All sizes reported in Table 2 and shown in Figure 3 use crystallite sizes as calculated from XRD.

The simulation assumes a perfectly spherical QD with an undistorted Ge lattice structure; faceted termination planes would lead to a reduction in the amplitudes from the simulated values. From this standpoint, the amplitude values are in agreement with the simulations. Second shell values for Ge edge data are lower than the calculations for a crystalline QD; however, if up to 20% of the Ge is in an amorphous state, the agreement is reasonable. In comparison, the smaller number of neighbors around the dopant atoms suggests that Bi atoms are more affected by surface effects and disorder than the Ge atoms are. On the basis of the data, it is likely that Bi primarily occupies lattice sites at the surface or on grain boundaries in the QDs.

To understand how surface site occupation would affect amplitude, the number of neighbors for a Bi atom sitting on three possible Ge surfaces was simulated by using Python code.



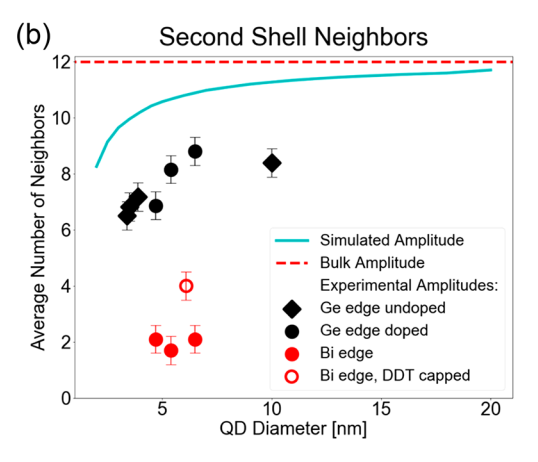


Figure 3. Simulated (a) first-shell and (b) second-shell amplitudes for QDs of various sizes. The simulation constructs a perfectly spherical particle of an undistorted Ge lattice. Amplitudes from data fits are overlaid Ge edge of pure QDs (black circles), Ge edge of doped QDs (black diamonds), Bi edge of doped QDs (red circles), and Bi edge of DDT capped QDs (open red circles).

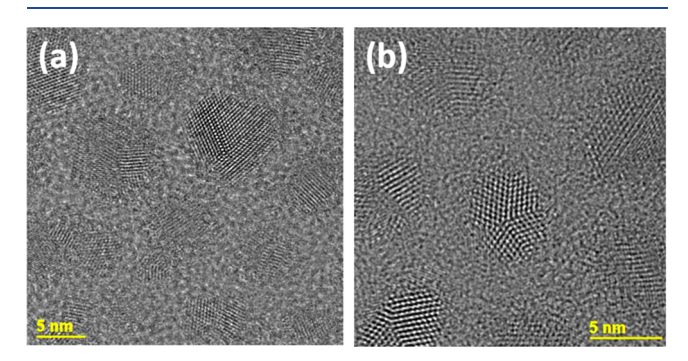


Figure 4. High-resolution transmission electron microscopy (HRTEM) images (a, b) show twinning, surface edges, and grain boundaries in 0.50 mol % Bi QDs capped with DDT; these features also are present in pure Ge QDs. Grain boundaries act as surfaces and may also be the site of Bi atoms.

Figure 5 shows the calculated number of neighbors for the first, second, and third nearest neighbors for the (100), (110), and (111) planes. Nearest-neighbor Bi—Ge bonds at the surface were expanded due to the larger size of the Bi atoms; the amount of expansion was adjusted to be the same as observed in the EXAFS data.

Simulation results show that the amplitude for surface Bi atoms would be between 2 and 3 on the first shell and 3 and 6 on

ACS Applied Nano Materials

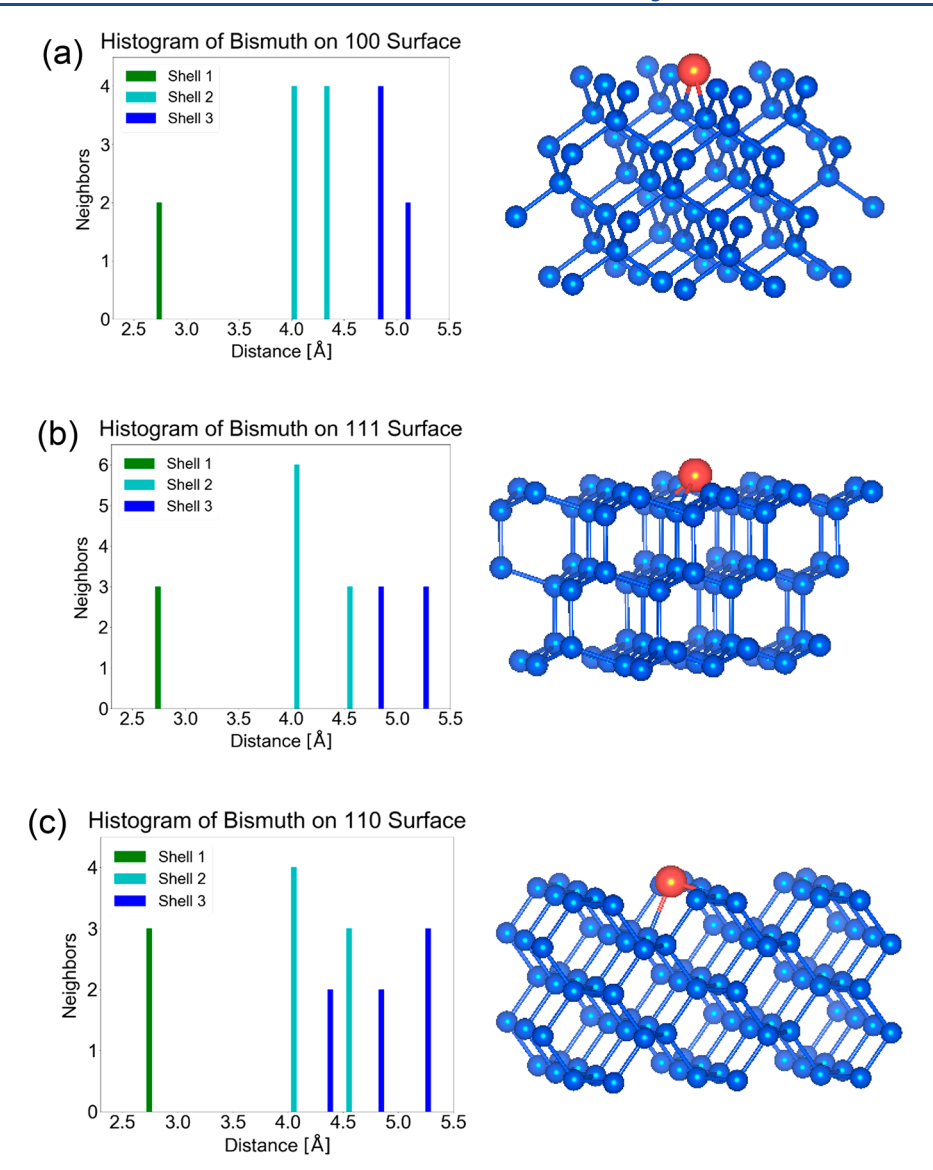


Figure 5. Histogram results for the simulations of the distances and number of neighbors for Bi atoms sitting on surface sites of the (a) (100), (b) (111), and (c) (110) planes. Simulations show peak splitting. Designation of the second or third shell is determined by where that neighbor would be in an undistorted lattice.

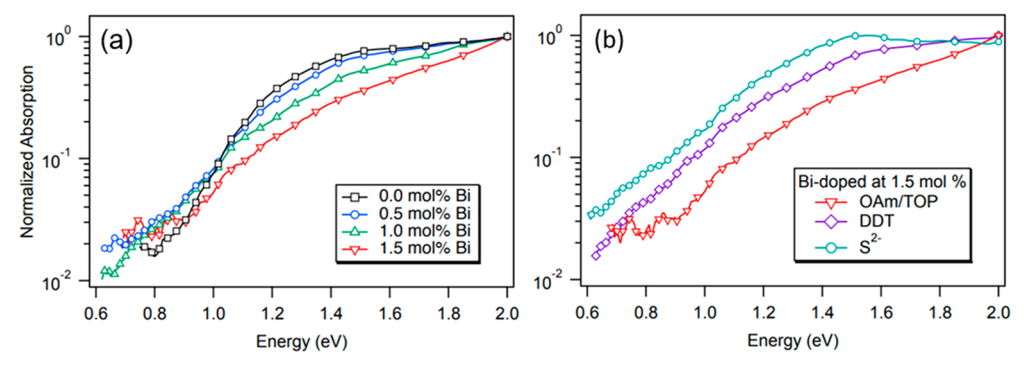


Figure 6. (a) PDS spectra for pure and doped QDs capped with OAm/TOP. Increasing Bi concentration results in higher Urbach energy, indicating greater disorder in the system. (b) 1.5% Bi-doped QDs capped with OAm/TOP, DDT, and sulfide ligands. After ligand exchange with DDT and S^{2-} , a significant amount of order is restored. EXAFS spectra of DDT-capped doped QDs showed an increase in structural order which is verified by the increase in optical order measured by PDS. The implication is that ligand exchange treatment and surface chemistry of these materials are critical to optimizing their application toward optoelectronic devices.

ACS Applied Nano Materials www.acsanm.org Article

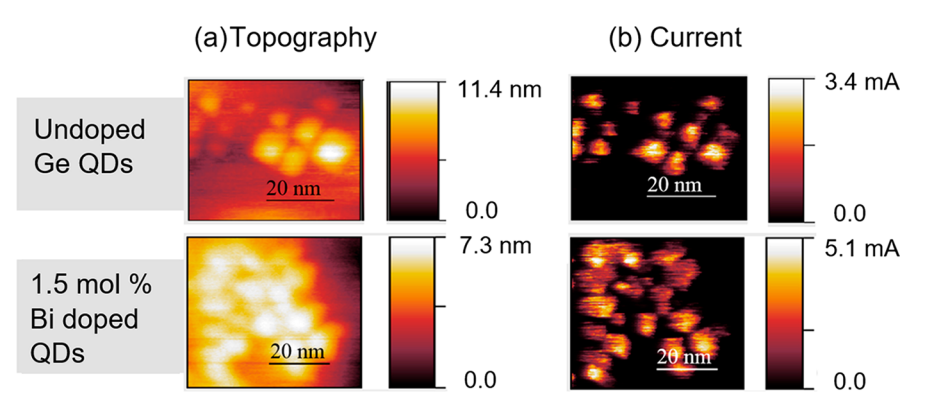


Figure 7. Conductive AFM (a) topography and (b) current maps for DDT-capped undoped and 1.5 mol % doped Ge QDs. Scale bars are equal to 20 nm.

data. Simulations also show splitting on the second- and thirdshell neighbors due to bond expansion along different lattice directions.

DFT simulations were run for Bi on the surface of the three planes; for each case, the surfaces were allowed to relax, and the resulting distributions of first second and third neighbors extracted. These pair distances and numbers of neighbors were used to fit the Bi-edge data. The amplitudes and pair distance shifts were fixed, and the peak widths were allowed to vary. However, the differences in the fits were not significant enough to differentiate between possible Bi sites.

Photothermal Deflection Spectroscopy (PDS). PDS was used to take detailed measurements of the absorption spectra of the QDs. PDS measures the deflection of a laser beam parallel to the surface of the sample, which is immersed in Fluorinert (C_6F_{14}) from 3M, used for its nonreactivity and large change in refractive index with small changes in temperature. As the sample is optically excited by a modulated monochromatic pump beam, the sample releases heat from nonradiative relaxation into the Fluorinert, creating a change in refractive index gradient. The mirage effect causes the tangential probe beam to be deflected in proportion to the sample absorption which is measured with a position-sensitive detector. The pump beam is scanned across wavelengths from above to below the bandgap. High sensitivity is achieved by locking-in the pump beam modulation. Because PDS measures the interaction of a tangential probe beam, the technique is insensitive to scattering or reflection artifacts. 39,40,53 PDS measurements were taken for samples drop-cast on glass slides, giving a varied thickness. This, combined with rough transmission measurements for scaling, led to a normalization of data at 2.0 eV, allowing order/disorder in each system to be compared. Measurements were repeated 3–5 times for verification of results.

PDS measures band-to-band absorption spectra, or in this case state-to-state, as the sample behaves as a quantum material. Figure 6 shows the absorption spectra for pure and doped Ge QDs capped with OAm/TOP ligands. The shoulder, most easily recognizable in pure and 0.5 mol % Bi-doped QDs, relates to a bandgap of ~0.95 eV. No shifts in bandgap were reported between samples although the shoulder is significantly rounded out with higher doping, obscuring changes in the bandgap. Fitting the shoulder region of PDS spectra can reveal the direct or indirect nature of the bandgap. However, the indistinct band edge of doped samples made it impossible to distinguish whether Bi doping caused a strain-induced conversion to a direct bandgap material.

Absorption decreases with lower photon energies following a linear exponential slope known as the Urbach energy, E_{uv} , which is an indicator of disorder. Urbach energies were extracted from PDS spectra by fitting the linear exponential tail of the absorption spectra to the following equation for absorbance: α $\sim \exp(E/E_{\rm u})$ where the slope is described by the Urbach energy, $E_{\rm u}$. The Urbach energy quantifies optical disorder which has important consequences on the optoelectronic performance of photoactive layer materials. Disorder-induced below-gap absorption increases the thermal generation rate and recombination centers. Thermal generation, recombination, and radiative emission compete with the ability of a material to convert photon energy to electrical energy. Open-circuit voltage, the driving force to separate charge carriers, is proportional to the ratio of the optical to thermal generation rate. Below-gap absorbance increases the thermal generation rate, therefore decreasing the open-circuit voltage. Recombination centers also have detrimental consequences to energy conversion by creating mid-gap trap states which act as recombination centers, preventing charge carrier separation and reducing current. 39,53,52

Perfect semiconductors have a discrete transition between absorption bands; however, conventional crystalline semiconductors have small amounts of band tailing (\sim 10 meV for crystalline Si) due to temperature-induced disorder. The structural disorder in amorphous semiconductors causes band tailing in the density of states for electrons caught in static random potentials. Urbach energies of >60 meV were measured for amorphous Si by Cody et al. 54

QDs have additional sources of disorder attributed to high numbers of trap states, surface area, and size polydispersity. Capping ligands have been shown to cause deviations from periodic lattice arrangements by altering the bond lengths on the nanocrystal surface. Consequently, Urbach energies for some nanomaterials have been reported in the hundreds of meV. Through improvements in processing conditions and capping ligands, much lower Urbach energies have been achieved for QD systems such as PbS. 40,55

The PDS measurements of OAm/TOP-capped Ge QDs show increasing Urbach energy with increasing Bi doping: 243 meV (no Bi doping), 365 meV (0.50 mol % Bi), 439 meV (1.0 mol % Bi), and 518 meV (1.5 mol % Bi). Bi incorporation introduces lattice distortions which is reflected in the higher values of the Urbach energy and is consistent with the EXAFS results reported above. A comparison of Urbach energy for 1.5 mol % Bi-doped Ge QDs before and after ligand exchange can be seen in Figure 6b. Here, we again see results consistent with EXAFS;

the original ligand, OAm/TOP, shows extreme disorder and a high Urbach energy. After exchange with either DDT or $\rm S^{2-}$, we see a restoration of order possibly due to the removal of loosely bonded, amorphous Bi at the surface of the QD while the majority of Bi dopant atoms remain incorporated into the surface of the host crystal lattice. As high levels of disorder are indicative of a lower $V_{\rm oc}$ we see an implication that the surface chemistry of these materials is critical to optimizing their application toward optoelectronic devices. 40

Transmission Electron Microscopy (TEM). Particle size distributions were measured with STEM and are shown in Figure S7. Particle sizes were found to be larger than crystallite size due to the presence of grain boundaries as seen in the HRTEM images (Figure 4). Crystallite sizes, reported in Table 2, were derived from XRD peak widths by using Scherrer analysis which does not reveal the size distribution. Particle sizes from TEM/STEM give a better indication of the polydispersity within a sample but are not a direct measurement of crystallite size distribution. TEM/STEM micrographs show that doped samples have an increase in size polydispersity with higher doping. Size polydispersity is an important source of Urbach energy at higher doping levels. As bandgap is controlled by size in the quantum regime, size polydispersity causes bandgap polydispersity and results in the rounding of the band edge (the shoulder) of the PDS spectra. This effect is observed in the disappearance of the spectrum shoulder at \sim 1.4 eV.

Conductive AFM. Conductive AFM (C-AFM) was taken of drop-cast films of QDs on ITO-coated glass, and current through individual QDs was measured under applied voltage. Topography and current maps of pure and doped, DDT-capped QDs are shown in Figure 7. DDT-capped QDs have greater stability in air, making them more appropriate for this technique. Current measurements were taken under 100 mV in ambient conditions in tapping mode to prevent QD displacement on the substrate by the AFM tip. Because of the relatively large size of conductive probes, topography measurements are skewed large. The maps show topography consistent with current measurements; 1.5 mol % Bi-doped Ge QDs have a higher maximum current of 5.1 nA when compared with pure Ge QDs, with a maximum current of 3.4 nA.

Device Results. Film conductivity of pure Ge, 1 mol % Bi, and 1.5 mol % Bi-doped Ge QDs was measured by fabricating heterojunction devices and extracting J-V curves as shown in Figure 8. Transport occurs in QD thin films via a hopping mechanism due to tunneling barriers caused by organic ligands

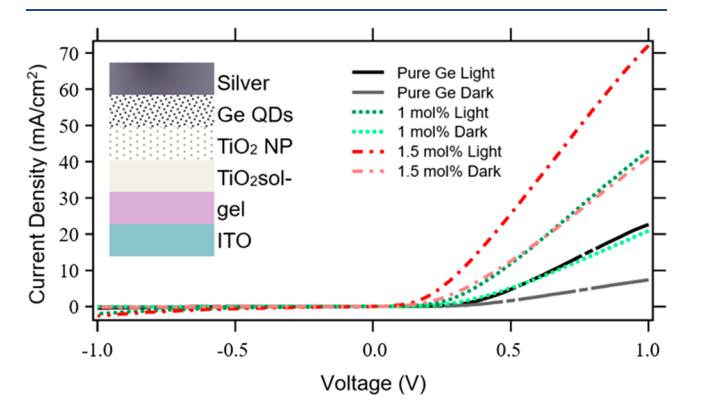


Figure 8. Dark and light J-V curves for devices as a function of Bi mol %. Dark currents and photocurrents increase with higher doping concentration.

on the QD surface. The S^{2-} -capped QD were chosen for two reasons. First, PDS spectra showed restoration of order after ligand exchange; this indicated a reduction in trap states which would increase charge carrier extraction. Second, short inorganic ligands decrease interdot spacing, which allows greater electronic wave function overlap and reduces barrier height. 56

Despite the high disorder found in the PDS measurements, devices behave as diodes and show increased dark current and photocurrent with doping; the extracted conductivity values are shown in Table 3. As the Urbach energy has several sources,

Table 3. Conductivity Values for Pure and Bi-Doped QDs Extracted from J-V Curves Shown in Figure 8

mol % Bi	dark current (Ω^{-1})	photocurrent (Ω^{-1})
0	11.4	36.1
1.0	31.0	62.5
1.5	56.9	94.3

structural disorder-induced trap states and crystallite size polydispersity being primary contributors, the increase in current density with doping indicates that trap states are not dominant at higher doping levels. The increase in dark current indicates higher levels of film conductivity which is known to increase carrier lifetime and extraction. Higher photocurrents measured are due to the increase in the number of electrons promoted to the conduction state under light. The absence of an open-circuit voltage is likely the result of a poor device architecture and an energy mismatch between the two electrodes with the Bi-doped Ge QD conduction and valence bands. The increase in photocurrents reported here provides positive implications for Bi-doped Ge QDs photovoltaic devices once a proper device architecture is found.

CONCLUSION

I

Bi dopants were shown to be incorporated into the Ge QD structure, primarily by occupying surface substitutional sites, as shown by fits to the Bi L₂ -edge EXAFS data using FEFF7 calculated paths. In particular, there are well-defined secondand third-neighbor peaks indicating an ordered structure, which would not occur for Bi randomly attached to the QD. The nearest-neighbor Bi-Ge bond is long, as expected from the larger covalent radii of Bi, and too long to fit inside the Ge lattice. The Bi-edge EXAFS amplitudes were significantly lower than those of the Ge edge, suggesting that Bi atoms primarily occupy lattice sites on the surface of the QD or in grain boundaries. Bi has no solubility in bulk Ge, and the results reported here indicate that nanocrystal surfaces offer a platform for formation of doped structures unachievable in bulk materials. While it was found that disorder increased with dopant concentration, ligand exchange partially restored order. This indicates the possibility of using chemical surface treatments to reduce surface trap states and should be explored further. Despite a rise in size polydispersity, Bi doping also increases both the dark current and photocurrent as measured by conductive AFM and I-Vcurves on heterojunction devices. These results show promise in using doping as a method to improve the performance of group IV QDs for use in optoelectronic devices such as photovoltaics, photodetectors, and diodes. Further studies will explore transport mechanisms such as mobility and carrier enhancement in electronic devices.

ASSOCIATED CONTENT

Supporting Information

The Supporting Information is available free of charge at https://pubs.acs.org/doi/10.1021/acsanm.0c00709.

Additional FTIR, EXAFS, XRD, TEM, PXRD, and PDS characterization, details on simulations procedures, Urbach energies, and calculated conductivities (PDF)

AUTHOR INFORMATION

Corresponding Author

Sue A. Carter — Department of Physics, University of California, Santa Cruz, Santa Cruz, California 95064, United States;
orcid.org/0000-0002-6233-6250; Email: sacarter@ucsc.edu

Authors

Heather Renee Sully — Department of Electrical Engineering, University of California, Santa Cruz, Santa Cruz, California 95064, United States; o orcid.org/0000-0001-7463-2543

Katayoon Tabatabaei — Department of Chemistry, University of California, Davis, Davis, California 95616, United States;
orcid.org/0000-0002-0694-4307

Kaitlin Hellier — Department of Physics, University of California, Santa Cruz, Santa Cruz, California 95064, United States; orcid.org/0000-0002-6328-1167

Kathryn A. Newton — Department of Chemistry, University of California, Davis, Davis, California 95616, United States; orcid.org/0000-0001-6117-4598

Zheng Ju − Department of Chemistry, University of California, Davis, Davis, California 95616, United States; ocid.org/0000-0002-5411-6952

Logan Knudson – Department of Physics, University of California, Santa Cruz, Santa Cruz, California 95064, United States

Shayan Zargar — Department of Physics, University of California, Santa Cruz, Santa Cruz, California 95064, United States;
orcid.org/0000-0002-3422-3355

Minyuan Wang – Department of Chemistry, University of California, Davis, Davis, California 95616, United States

Susan M. Kauzlarich — Department of Chemistry, University of California, Davis, Davis, California 95616, United States;
ocid.org/0000-0002-3627-237X

Frank Bridges — Department of Physics, University of California, Santa Cruz, Santa Cruz, California 95064, United States

Complete contact information is available at: https://pubs.acs.org/10.1021/acsanm.0c00709

Notes

The authors declare no competing financial interest.

ACKNOWLEDGMENTS

This work was supported by the National Science Foundation (Grant CHE-1710110). The EXAFS experiments were performed at the Stanford Synchrotron Radiation Lightsource (SSRL), which is supported by the U.S. Department of Energy, Office of Science, Office of Basic Energy Sciences, under Contract DE-AC02-76SF00515. We thank the Advanced Materials Characterization and Testing Laboratory at UC Davis for the use of the transmission and scanning transmission electron microscope. We thank Yuan Ping and Chunhao Guo for running simulations of Bi on the surface of the (111), (110), and

(100) lattice planes. We thank Sara Ostrowski of EAG Laboratories for taking conductive AFM measurements.

REFERENCES

- (1) Talapin, D. V.; Lee, J.-S.; Kovalenko, M. V.; Shevchenko, E. V. Prospects of Colloidal Nanocrystals for Electronic and Optoelectronic Applications. *Chem. Rev.* **2010**, *110* (1), 389–458.
- (2) Stavrinadis, A.; Rath, A. K.; de Arquer, F. P. G.; Diedenhofen, S. L.; Magen, C.; Martinez, L.; So, D.; Konstantatos, G. Heterovalent Cation Substitutional Doping for Quantum Dot Homojunction Solar Cells. *Nat. Commun.* **2013**, *4* (1), 1–7.
- (3) Makkar, M.; Viswanatha, R. Frontier Challenges in Doping Quantum Dots: Synthesis and Characterization. *RSC Adv.* **2018**, 8 (39), 22103–22112.
- (4) Vaughn, D. D., II; Schaak, R. E. Synthesis, Properties and Applications of Colloidal Germanium and Germanium-Based Nanomaterials. *Chem. Soc. Rev.* **2013**, 42 (7), 2861–2879.
- (5) Tabatabaei, K.; Lu, H.; Nolan, B. M.; Cen, X.; McCold, C. E.; Zhang, X.; Brutchey, R. L.; van Benthem, K.; Hihath, J.; Kauzlarich, S. M. Bismuth Doping of Germanium Nanocrystals through Colloidal Chemistry. *Chem. Mater.* **2017**, *29* (17), 7353–7363.
- (6) Ruddy, D. A.; Johnson, J. C.; Smith, E. R.; Neale, N. R. Size and Bandgap Control in the Solution-Phase Synthesis of Near-Infrared-Emitting Germanium Nanocrystals. *ACS Nano* **2010**, *4* (12), 7459–7466
- (7) Gao, Y.; Pi, X.; Wang, X.; Yuan, T.; Jiang, Q.; Gresback, R.; Lu, J.; Yang, D. Structures, Oxidation, and Charge Transport of Phosphorus-Doped Germanium Nanocrystals. *Part. Part. Syst. Charact.* **2016**, 33 (5), 271–278.
- (8) Norris, D. J.; Efros, A. L.; Erwin, S. C. Doped Nanocrystals. *Science* **2008**, *319* (5871), 1776–1779.
- (9) Cao, Y. C. Impurities Enhance Semiconductor Nanocrystal Performance. *Science* **2011**, 332 (6025), 48–49.
- (10) Wills, A. W.; Kang, M. S.; Wentz, K. M.; Hayes, S. E.; Sahu, A.; Gladfelter, W. L.; Norris, D. J. Synthesis and Characterization of Al- and In-Doped CdSe Nanocrystals. *J. Mater. Chem.* **2012**, 22 (13), 6335–6342.
- (11) Mocatta, D.; Cohen, G.; Schattner, J.; Millo, O.; Rabani, E.; Banin, U. Heavily Doped Semiconductor Nanocrystal Quantum Dots. *Science* **2011**, 332 (6025), 77–81.
- (12) Engel, J. H.; Alivisatos, A. P. Postsynthetic Doping Control of Nanocrystal Thin Films: Balancing Space Charge to Improve Photovoltaic Efficiency. *Chem. Mater.* **2014**, 26 (1), 153–162.
- (13) Tang, J.; Konstantatos, G.; Hinds, S.; Myrskog, S.; Pattantyus-Abraham, A. G.; Clifford, J.; Sargent, E. H. Heavy-Metal-Free Solution-Processed Nanoparticle-Based Photodetectors: Doping of Intrinsic Vacancies Enables Engineering of Sensitivity and Speed. *ACS Nano* **2009**, 3 (2), 331–338.
- (14) Barrows, C. J.; Chakraborty, P.; Kornowske, L. M.; Gamelin, D. R. Tuning Equilibrium Compositions in Colloidal $Cd_{1.x}Mn_xSe$ Nanocrystals Using Diffusion Doping and Cation Exchange. *ACS Nano* **2016**, *10* (1), 910–918.
- (15) Stavrinadis, A.; Pelli Cresi, J. S.; d'Acapito, F.; Magén, C.; Boscherini, F.; Konstantatos, G. Aliovalent Doping in Colloidal Quantum Dots and Its Manifestation on Their Optical Properties: Surface Attachment versus Structural Incorporation. *Chem. Mater.* 2016, 28 (15), 5384–5393.
- (16) Law, M.; Luther, J. M.; Song, Q.; Hughes, B. K.; Perkins, C. L.; Nozik, A. J. Structural, Optical, and Electrical Properties of PbSe Nanocrystal Solids Treated Thermally or with Simple Amines. *J. Am. Chem. Soc.* **2008**, *130* (18), 5974–5985.
- (17) Kolobov, A. V.; Oyanagi, H.; Wei, S.; Brunner, K.; Abstreiter, G.; Tanaka, K. Local Structure of Ge Quantum Dots Self-Assembled on Si(100) Probed by x-Ray Absorption Fine-Structure Spectroscopy. *Phys. Rev. B: Condens. Matter Mater. Phys.* **2002**, DOI: 10.1103/PhysRevB.66.075319.
- (18) Oliva-Chatelain, B. L.; Ticich, T. M.; Barron, A. R. Doping Silicon Nanocrystals and Quantum Dots. *Nanoscale* **2016**, 8 (4), 1733–1745.

- (19) Yuan, T. H.; Pi, X. D.; Yang, D. Nonthermal Plasma Synthesized Boron-Doped Germanium Nanocrystals. *IEEE J. Sel. Top. Quantum Electron.* **2017**, 23 (5), 1–5.
- (20) Xiu, F. X.; Yang, Z.; Mandalapu, L. J.; Zhao, D. T.; Liu, J. L.; Beyermann, W. P. High-Mobility Sb-Doped p-Type ZnO by Molecular-Beam Epitaxy. *Appl. Phys. Lett.* **2005**, *87* (15), 152101.
- (21) Kompch, A.; Sahu, A.; Notthoff, C.; Ott, F.; Norris, D. J.; Winterer, M. Localization of Ag Dopant Atoms in CdSe Nanocrystals by Reverse Monte Carlo Analysis of EXAFS Spectra. *J. Phys. Chem. C* **2015**, *119* (32), 18762–18772.
- (22) Chen, D.; Viswanatha, R.; Ong, G. L.; Xie, R.; Balasubramaninan, M.; Peng, X. Temperature Dependence of "Elementary Processes" in Doping Semiconductor Nanocrystals. *J. Am. Chem. Soc.* **2009**, *131* (26), 9333–9339.
- (23) Carolan, D.; Doyle, H. Size Controlled Synthesis of Germanium Nanocrystals: Effect of Ge Precursor and Hydride Reducing Agent. *J. Nanomater.* **2015**, *16* (1), 1–9.
- (24) Bernard, A.; Zhang, K.; Larson, D.; Tabatabaei, K.; Kauzlarich, S. M. Solvent Effects on Growth, Crystallinity, and Surface Bonding of Ge Nanoparticles. *Inorg. Chem.* **2018**, *57* (9), 5299–5306.
- (25) Muthuswamy, E.; Zhao, J.; Tabatabaei, K.; Amador, M. M.; Holmes, M. A.; Osterloh, F. E.; Kauzlarich, S. M. Thiol-Capped Germanium Nanocrystals: Preparation and Evidence for Quantum Size Effects. *Chem. Mater.* **2014**, *26* (6), 2138–2146.
- (26) Baldwin, R. K.; Pettigrew, K. A.; Garno, J. C.; Power, P. P.; Liu, G.; Kauzlarich, S. M. Room Temperature Solution Synthesis of Alkyl-Capped Tetrahedral Shaped Silicon Nanocrystals. *J. Am. Chem. Soc.* **2002**, *124* (7), 1150–1151.
- (27) Tabatabaei, K.; Holmes, A. L.; Newton, K. A.; Muthuswamy, E.; Sfadia, R.; Carter, S. A.; Kauzlarich, S. M. Halogen-Induced Crystallinity and Size Tuning of Microwave Synthesized Germanium Nanocrystals. *Chem. Mater.* **2019**, *31* (18), 7510–7521.
- (28) Baldwin, R. K.; Zou, J.; Pettigrew, K. A.; Yeagle, G. J.; Britt, R. D.; Kauzlarich, S. M. The Preparation of a Phosphorus Doped Silicon Film from Phosphorus Containing Silicon Nanoparticles. *Chem. Commun.* **2006**, No. *6*, 658–660.
- (29) McLeod, M.; Tabor, C. Tunable Conductivity of Germanium Thin Films Fabricated via Doped Colloidal Nanoparticle Sintering. *J. Phys. Chem. C* **2019**, 123 (2), 1477–1482.
- (30) Ruddy, D. A.; Erslev, P. T.; Habas, S. E.; Seabold, J. A.; Neale, N. R. Surface Chemistry Exchange of Alloyed Germanium Nanocrystals: A Pathway Toward Conductive Group IV Nanocrystal Films. *J. Phys. Chem. Lett.* **2013**, *4* (3), 416–421.
- (31) Esteves, R. J. A.; Ho, M. Q.; Arachchige, I. U. Nanocrystalline Group IV Alloy Semiconductors: Synthesis and Characterization of Quantum Dots for Tunable Bandgaps. *Chem. Mater.* **2015**, 27 (5), 1559–1568.
- (32) Demchenko, D. O.; Tallapally, V.; Esteves, R. J. A.; Hafiz, S.; Nakagawara, T. A.; Arachchige, I. U.; Özgür, Ü. Optical Transitions and Excitonic Properties of Alloy Quantum Dots. *J. Phys. Chem. C* **2017**, *121* (33), 18299–18306.
- (33) Zhang, D.; Jin, L.; Liao, Y.; Liu, Y.; Wen, T. Infrared and Terahertz Modulation Characteristics of N-GeBi/p-Si Photodiodes. *IEEE Trans. Electron Devices* **2017**, *64* (1), 176–181.
- (34) Peter, Y. U. Fundamentals of Semiconductors Physics and Materials Properties; https://www.springer.com/us/book/9783642007095 (accessed February 27, 2019).
- (35) Buonsanti, R.; Milliron, D. J. Chemistry of Doped Colloidal Nanocrystals. *Chem. Mater.* **2013**, 25 (8), 1305–1317.
- (36) Pugsley, A. J.; Bull, C. L.; Sella, A.; Sankar, G.; McMillan, P. F. XAS/EXAFS Studies of Ge Nanoparticles Produced by Reaction between Mg2Ge and GeCl4. *J. Solid State Chem.* **2011**, *184* (9), 2345–2352.
- (37) Davis, S. R.; Chadwick, A. V.; Wright, J. D. A Combined EXAFS and Diffraction Study of Pure and Doped Nanocrystalline Tin Oxide. *J. Phys. Chem. B* **1997**, *101* (48), 9901–9908.
- (38) Gul, S.; Cooper, J. K.; Corrado, C.; Vollbrecht, B.; Bridges, F.; Guo, J.; Zhang, J. Z. Synthesis, Optical and Structural Properties, and

- Charge Carrier Dynamics of Cu-Doped ZnSe Nanocrystals. J. Phys. Chem. C 2011, 115 (43), 20864–20875.
- (39) Guyot-Sionnest, P.; Lhuillier, E.; Liu, H. A Mirage Study of CdSe Colloidal Quantum Dot Films, Urbach Tail, and Surface States. *J. Chem. Phys.* **2012**, *137* (15), 154704.
- (40) Jean, J.; Mahony, T. S.; Bozyigit, D.; Sponseller, M.; Holovský, J.; Bawendi, M. G.; Bulović, V. Radiative Efficiency Limit with Band Tailing Exceeds 30% for Quantum Dot Solar Cells. *ACS Energy Lett.* **2017**, 2 (11), 2616–2624.
- (41) Boles, M. A.; Ling, D.; Hyeon, T.; Talapin, D. V. Erratum: The Surface Science of Nanocrystals. *Nat. Mater.* **2016**, *15* (3), 364–364.
- (42) Kroupa, D. M.; Vörös, M.; Brawand, N. P.; McNichols, B. W.; Miller, E. M.; Gu, J.; Nozik, A. J.; Sellinger, A.; Galli, G.; Beard, M. C. Tuning Colloidal Quantum Dot Band Edge Positions through Solution-Phase Surface Chemistry Modification. *Nat. Commun.* **2017**, 8 (1), 15257.
- (43) Brown, P.; Kim, D.; Lunt, R.; Zhao, N.; Bawendi, M.; et al. Energy Level Modification in Lead Sulfide Quantum Dot Thin Films through Ligand Exchange. *ACS Nano* **2014**, *8* (6), 5863–5872.
- (44) Munro, A.; Zacher, B.; Graham, A.; Armstrong, N. Photoemission Spectroscopy of Tethered CdSe Nanocrystals: Shifts in Ionization Potential and Local Vacuum Level As a Function of Nanocrystal Capping Ligand. ACS Appl. Mater. Interfaces 2010, 2 (3), 863–869.
- (45) Santra, P.; Palmstrom, A.; Tanskanen, J.; Yang, N.; Bent, S. Improving Performance in Colloidal Quantum Dot Solar Cells by Tuning Band Alignment through Surface Dipole Moments. *J. Phys. Chem. C* **2015**, *119* (6), 2996–3005.
- (46) Schleder, G.; Azevedo, G.; Nogueira, I.; Rebelo, Q.; Bettini, J.; Fazzio, A.; Leite, E. Decreasing Nanocrystal Structural Disorder by Ligand Exchange: An Experimental and Theoretical Analysis. *J. Phys. Chem. Lett.* **2019**, *10* (7), 1471–1476.
- (47) Booth, C. H. R-Space X-Ray Absorption Package, 2010.
- (48) Ankudinov, A. L.; Rehr, J. J. Relativistic Calculations of Spin-Dependent x-Ray-Absorption Spectra. *Phys. Rev. B: Condens. Matter Mater. Phys.* **1997**, *56* (4), R1712–R1716.
- (49) Gwyddion: an open-source software for SPM data analysis: Open Physics; https://www.degruyter.com/view/j/phys.2012.10.issue-1/s11534-011-0096-2/s11534-011-0096-2.xml?lang=en (accessed February 10, 2020).
- (50) Arango, A. C.; Johnson, L. R.; Bliznyuk, V. N.; Schlesinger, Z.; Carter, S. A.; Hörhold, H.-H. Efficient Titanium Oxide/Conjugated Polymer Photovoltaics for Solar Energy Conversion. *Adv. Mater.* **2000**, 12 (22), 1689–1692.
- (51) Cooper, A. S. Precise Lattice Constants of Germanium, Aluminum, Gallium Arsenide, Uranium, Sulphur, Quartz and Sapphire. *Acta Crystallogr.* **1962**, *15* (6), 578–582.
- (52) Stern, E. A. Number of Relevant Independent Points in X-Ray-Absorption Fine-Structure Spectra. *Phys. Rev. B: Condens. Matter Mater. Phys.* **1993**, 48 (13), 9825–9827.
- (53) Aşıkoğlu, A.; Yükselici, M. H. Evolution of the Energy Band Structure in Chemical-Bath-Deposited CdS Thin Films Studied by Optical Absorption Spectroscopy. *Semicond. Sci. Technol.* **2011**, 26 (5), 055012.
- (54) Cody, G. D. Urbach Edge of Crystalline and Amorphous Silicon: A Personal Review. *J. Non-Cryst. Solids* **1992**, *141*, 3–15.
- (55) Barkhouse, D. A. R.; Pattantyus-Abraham, A. G.; Levina, L.; Sargent, E. H. Thiols Passivate Recombination Centers in Colloidal Quantum Dots Leading to Enhanced Photovoltaic Device Efficiency. *ACS Nano* **2008**, 2 (11), 2356–2362.
- (56) Kagan, C. R.; Murray, C. B. Charge Transport in Strongly Coupled Quantum Dot Solids. *Nat. Nanotechnol.* **2015**, *10* (12), 1013–1026.